

Breaking one into three: Surface-tension-driven droplet breakup in T-junctions

Jiande Zhou ¹, Yves-Marie Ducimetière ², Daniel Migliozi ¹, Ludovic Keiser ^{2,3},
Arnaud Bertsch ¹, François Gallaire ² and Philippe Renaud ¹

¹Laboratory of Microsystems (LMIS4), EPFL, CH1015 Lausanne, Switzerland

²Laboratory of Fluid Mechanics and Instabilities, EPFL, CH1015 Lausanne, Switzerland

³Université Côte d'Azur, CNRS, INPHYNI, France



(Received 1 July 2022; accepted 6 March 2023; published 16 May 2023)

Droplet breakup is an important phenomenon in the field of microfluidics to generate daughter droplets. In this work, a novel breakup regime in the widely studied T-junction geometry is reported, where the pinch-off occurs laterally in the two outlet channels, leading to the formation of three daughter droplets, rather than at the center of the junction for conventional T-junctions which leads to two daughter droplets. It is demonstrated that this new mechanism is driven by surface tension, and a design rule for the T-junction geometry is proposed. A model for low values of the capillary number Ca is developed to predict the formation and growth of an underlying carrier fluid pocket that accounts for this lateral breakup mechanism. At higher values of Ca , the conventional regime of central breakup becomes dominant again. The competition between the new and the conventional regime is explored. Altogether, this novel droplet formation method at T-junction provides the functionality of alternating droplet size and composition, which can be important for the design of new microfluidic tools.

DOI: [10.1103/PhysRevFluids.8.054201](https://doi.org/10.1103/PhysRevFluids.8.054201)

I. INTRODUCTION

Droplet formation is a ubiquitous process in both nature and industry. In the context of microfluidics, the controllable generation of microdroplets has enabled a wide range of applications, opening a new era for biological and chemical analysis and synthesis [1–3]. The formation of droplets is the first step to achieve in the pipeline in order to achieve versatile functionalities such as microreactors [4–6], mini-incubators [6–8], material templates [9–11], digital counters [12–14], or single cell platforms [15–18]. To date, droplet formation mechanisms in rectangular microchannels have been widely studied and can be classified in two main categories [19–24]: the mechanisms driven by hydrodynamic forces and those driven by surface tension. In the former category, the carrier flow is brought to the dispersed phase to generate viscous and/or inertial forces destabilizing the interface, and surface tension acts as the stabilizing force. In the latter, the interface breakup is purely driven by an imbalance in capillary pressure induced by an abrupt change of confinement [25]. The first category of droplet production processes is flexible in operation and advantageous in producing a high droplet throughput [6,22,26]. Although limited by the flow rate, the second category is advantageous for monodisperse droplet production and parallelization [27–29].

Droplet formation can result from the emulsification of a continuous phase or from the breakup of an existing droplet. The latter process enables us to adjust the initial droplet size to increase droplet production rate or to provide new functionalities, such as up-concentration [30,31]. One of the most studied geometries for droplet breakup is the T-junction, where a straight channel splits perpendicularly into two lateral channels. Following the seminal work by Link *et al.* [32], various studies have investigated the dynamics of the droplet breakup process for both short [33–39] and

elongated droplets [40–46]. Other studies also investigated how to modify the topography of the T-junction to perform asymmetric droplet breakup [47–49]. In all those configurations, droplets do not break up at small capillary numbers $Ca = \mu V/\gamma$ and are split into two daughter droplets above a critical capillary number $Ca_c = \mu V_c/\gamma$, with μ the viscosity of the carrier fluid, γ the interfacial tension, and V the speed of the droplet. The breakup process is here driven by the hydrodynamic stress exerted by the carrier flow which enables to deform and break the interface.

In this study, we report a novel droplet breakup regime in T-junctions that is surface-tension driven. In this regime, the droplet interface ruptures symmetrically in the two lateral channels away from the junction, which gives birth to three daughter droplets instead of two. We show that this regime only occurs in T-junctions that have a different aspect and width ratio compared to the ones presented so far in the scientific literature. The height h of the channels must be larger than the width of the inlet channel w_i , which itself must be larger than the width of the outlet channel w_o : $h > w_i > w_o$. We describe the underlying mechanism of the new droplet breakup mechanism and provide a geometry design rule predicting the occurrence of the new regime in a T-junction. We also propose a semiquantitative model accounting for the gutter flows to describe the dynamical process of the new breakup regime. Finally, we show that the conventional central breakup also occurs in the new T-junctions under certain flow conditions. Both central and lateral breakup regimes can develop independently, but the droplet breakup regime actually occurring is the faster one.

II. EXPERIMENTAL AND NUMERICAL METHODS

A. Device fabrication

To create the microchannels, a silicon mold fabricated by dry reactive ion etching (DRIE) was used. First, a 1.5- μm photoresist layer was deposited on double-side polished silicon wafers and was patterned with standard photolithography including steps of exposure and development to obtain the two-dimensional (2D) channel shape. The exposed wafer area was then etched using the Bosch process (DRIE, Alcatel AMS 200). The obtained channel depth is proportional to the etching duration, and the value is measured with a surface profilometer (Tencor Alpha-Step 500). After the Si mold was silanized within a desiccator filled with trichlor-(1H,1H,2H,2H-perfluorooctyl) (called PFOT in the following) for 5 h, we pour polydimethylsiloxane (PDMS) prepolymer (1:10 ratio mixture) onto the Si mold and cure in an 80° oven for 3 h. We peel the PDMS replicas from the mold and, after punching inlet and outlet holes, seal the channels by bonding to a PDMS-coated glass slide (oxygen plasma bonding, 500 mTorr, 45 s, 29 W). Coating of the glass slide (standard 25 × 75 × 1 mm) is done by spin coating a thin layer of PDMS prepolymer at 1700 rpm for 35 s, then curing in the oven (as above). The hydrophobicity of the surfaces was naturally regained by placing PDMS in the oven for 3 days.

B. Experiments

The experiments were performed under an inverted microscope (Nikon Eclipse TE 300) and imaged with a high-speed camera (Phantom Miro M310). Depending on the flow rates, frame rates up to 50 000 frames per second were used for recording the droplet breakup process. A customized ImageJ script is used to automatically recognize the droplets and obtain the intensity profile. A MATLAB (Mathworks) script is used for calculating the droplet speed and length. The results were confronted to the observations to ensure accuracy. To conduct the experiments, constant flow rates were fed to the system using CETONI Nemesys syringe pumps (low-pressure module, Cetoni GmbH, Germany), 100- μl gastight glass syringes (Hamilton 1700 Series), and Tygon tubings (Masterflex). To avoid possible fluctuations in the system, we used the actual droplet speed determined from the video to determine the capillary number. QX200 Droplet Generation Oil from Bio-Rad (containing surfactant) was used as the continuous phase to avoid droplet coalescence. Deionized water was used as the dispersed phase. The viscosity of the droplet generation oil was measured using a rheometer (DHR-3 TA): $\mu = 2.3 \text{ mPa s}$. The interfacial tension between the

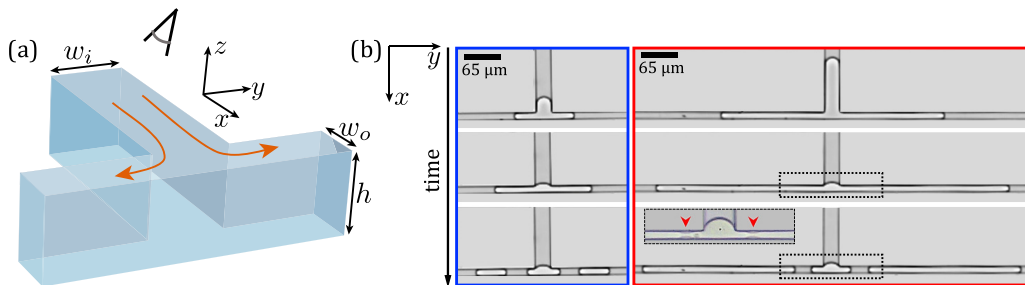


FIG. 1. (a) Geometry of the T-junctions used throughout our study: Both aspect ratio h/w_o and width ratio w_i/w_o are larger than unity. The eye shows the observation perspective during experiment. (b) Time sequence of a lateral breakup process for a short (blue) and a long (red) droplet. Inset shows the interface at the moment of rupture (red arrow), captured at a frame rate of 50 000 fps.

two phases (γ) was measured with the pendant drop method (Kruss Advance 1.6.2.0) and equals $\gamma = 1.6$ mN/m. The contact angle of water on PDMS was measured as 110° .

C. Numerical simulations

The closed system for the three unknowns $\bar{z}(\eta, t)$, $\bar{k}(\eta, t)$, and $L_p(t)$ from Eqs. (A5) and (A7) was solved numerically using the COMSOL Multiphysics software, based on the finite-element method. More precisely, the system (A5) is implemented directly in the “General form PDE” component of the software, and its weak form has been spatially discretized over the interval $\xi \in [0, 1]$ using first-order polynomials (corresponding to a linear interpolation of the solution). The convergence of the numerical results with respect to the spatial discretization has been verified. Equation (A7), enforcing the volume conservation thus depending only on time, is implemented in the “Global Equations” component. The system is marched in time using the backward differentiation formula, and the results are sought for 4000 discrete times uniformly distributed between 0 and $10/\text{Ca}$. A stopping condition has been added, such that the simulation stops running if $\min(\bar{z}) < 1/2$. Concerning the nonlinear, fully coupled solver, the default choices of COMSOL parameters have been found sufficient for convergence, excepted the “Jacobian update” that is set to “updated on every iteration” and the “maximum number of iterations” that is set to 500.

III. RESULTS

A. Description of a novel breakup mechanism

In previous studies, droplet breakup was conducted in T-junctions, where the inlet and outlet channels have the same width and where the channel height is equal to or smaller than the width [32,34,44]. In this study, we use a nonconventional T-junction [Fig. 1(a)] with the inlet and outlet width (w_i and w_o , respectively) and the height of the channel (h) fulfilling $h > w_i > w_o$. Consequently, both the aspect ratio (h/w_o) and the width ratio (w_i/w_o) are larger than unity. Upstream of the T-junction, water-in-oil droplets are generated using a flow-focusing device with two inlets, one introducing deionized water (dispersed phase) and the other fluorinated oil (continuous phase). A third inlet introduces additional oil downstream of the flow-focusing unit in order to separate the droplets and further control their speed. When a droplet passes through the T-junction and fully enters the lateral channels, its rear interface remains pinned at the junction with a constant and convex curvature, whereas the front interfaces advance further downstream. This is in contrast with the central breakup mechanism which features a progressive concave curving of the rear interface during breakup [32]. Eventually, it is the interfaces inside the lateral channels that collapse and create two new interfaces at a symmetric distance from the junction. This type of breakup

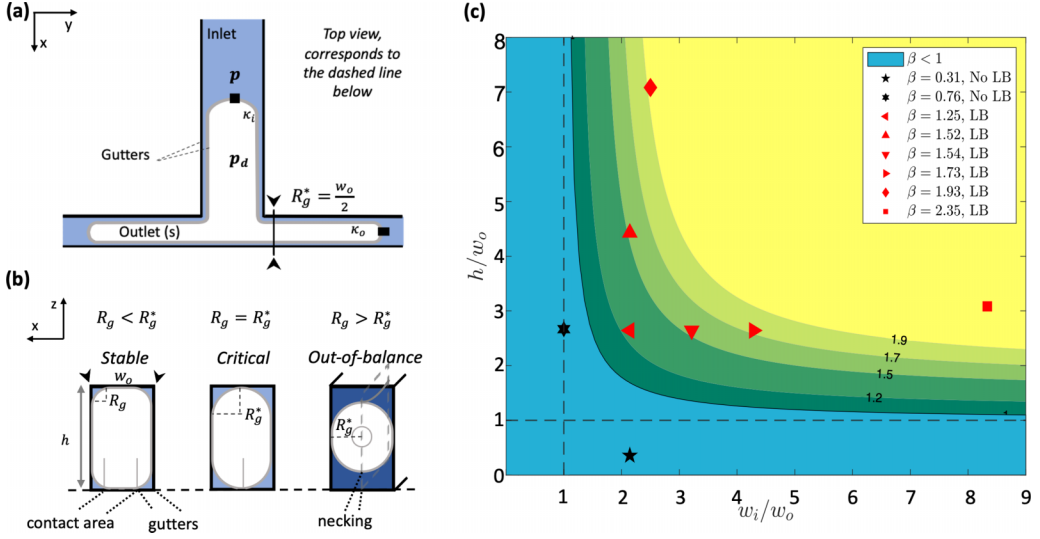


FIG. 2. Capillary instability responsible for lateral breakup. (a) Presentation of key droplet parameters with a top view of a T-junction through which a droplet splits. (b) Cross-sectional view in the outlet channel [indicated by black arrowheads in (a)] showing three different gutter radius. These three conditions can hold for the same droplet passing the junction at different times. When $R_g > R_g^*$, the necking starts. (c) Colormap representing β in a diagram representing the aspect ratio h/w_o as a function of the width ratio w_i/w_o . Blue region corresponds to $\beta < 1$, i.e., geometries that does *not* allow the occurrence of lateral breakup; green regions correspond to $\beta > 1$, i.e., geometries prone to exhibit lateral breakup. Each marker corresponds to one of the geometries experimentally tested (see Table I). A black symbol corresponds to an absence of lateral breakup observed, and a red marker corresponds to a presence of a lateral breakup.

creates three daughter droplets rather than two (which is observed during the classical breakup at T-junction). This breakup is referred to as *lateral breakup*, in comparison to the classical *central breakup* described in the literature. Two examples of droplets undergoing a lateral breakup are presented in Fig. 1(b). The collapse is very rapid but can be captured by a high speed camera (inset).

The interface appears to break suddenly during the time the rear cap remains pinned at the junction. It suggests that the necking process, which is usually more gradual, is likely acting off-plane before the final pinch-off happens.

B. Geometric conditions required for the lateral breakup

We first detail the geometry of the T-junction which enables the lateral breakup phenomenon. Using a quasistatic assumption, we consider that the Young-Laplace equation controls the pressure drop across the interface of the droplet: $p_d - p = \gamma\kappa$, where p_d is the pressure in the drop, p is the pressure in the surrounding fluid at the interface [Fig. 2(a)], γ is the interfacial tension, and κ is the local mean curvature of the interface. When the droplet passes through a T-junction whose outlet channels have smaller dimension than the inlet channel ($w_o < w_i$), the curvature at the front of the droplet κ_o increases compared to the curvature at the rear κ_i , thereby creating a pressure gradient along the droplet interface. We assume that the dominant pressure variations occur in the gutters present in the corners of the cross section and consider that the pressure in the droplet p_d can be roughly considered as constant in space and time [44,50]. It implies that in the fluid surrounding the droplet, the pressure gradually decreases from the rear cap in the inlet channel ($p_i = p_d - \gamma\kappa_i$) to the front cap in the outlet channels ($p_o = p_d - \gamma\kappa_o$), by continuity. This pressure gradient is accompanied by an adaptation of the radius of the gutter R_g , such that $p = p_d - \gamma/R_g$. Along the droplet, R_g thus varies from $1/\kappa_i$ in the rear of the droplet to $1/\kappa_o$ in the front. In the quasistatic

TABLE I. Tested geometries and the corresponding breakup outcome.

Geometry	w_i (μm)	w_o (μm)	h (μm)	h/w_o	w_i/w_o	k_i	β	$L(0)/w_i$	Ca range	LB
A	30	14	62	4.2	2.1	0.09	1.5	2.8–10	0.005–0.30	Yes
B	30	14	37	2.6	2.1	0.11	1.2	2.8–5.9	0.006–0.077	Yes
C	30	14	5	0.4	2.1	0.45	0.3	1.2–9.5	0.006–0.107	No
D	60	14	37	2.6	4.3	0.08	1.7	1.0–4.8	0.004–0.183	Yes
E	45	14	37	2.6	3.2	0.09	1.5	1.4–2.1	0.014–0.138	Yes
F	30	30	80	2.8	1	0.09	0.8	—	0.006–0.160	No
G	100	12	37	3.1	8.3	0.07	2.4	0.9–3.1	0.035–0.73	Yes
H	30	12	85	7.1	2.5	0.09	1.9	1.6–8.5	0.02–0.04	Yes

condition, the value of κ_i and κ_o is constant and only dependent on the channel geometry [51]:

$$\kappa_{i,o} = \frac{1 + \frac{w_{i,o}}{h} + \sqrt{\left[\left(1 - \frac{w_{i,o}}{h}\right)^2 + \pi \frac{w_{i,o}}{h}\right]}}{w_{i,o}}. \quad (1)$$

where i and o respectively account for inlet and outlet. However, due to the confinement and the nonwetting condition, R_g cannot exceed a threshold value given by half of the smallest dimension of the cross section [27]. In our case $w_o < h$, which gives a critical value R_g^* in the outlet channel: $R_g^* = w_o/2$. Consequently, if the relatively large pressure imposed in the gutter by the proximity of the rear cap imposes a radius of curvature R_g larger than R_g^* in the outlet channels, then an instability is triggered [Fig. 2(b)]. In order to fulfill the continuity of pressure along the channel, the interface has to curve concavely in the y direction, which marks the initiation of a necking process. A ‘‘pocket’’ thus gradually inflates at the upper and bottom part of the channel between the droplet and the (x, y) walls, where the continuous phase accumulates. The droplet thereby thins down (necking process) until reaching a quasicylindrical shape, when surface tension induces a final and sudden breakup. Such a necking process is off-plane until the last moment of rupture, which is in consistence with the experimental observation. The lateral breakup most often occurs simultaneously in both outlet channels.

Note that the necking criterion $R_g > R_g^* = w_o/2$ is analogous to the one-ruling-step emulsification [25] or snap-off [52] processes. The geometric criterion for a T-junction to allow a passing droplet meet the necking condition of $R_g > R_g^*$ can be expressed as $1/\kappa_i > R_g^*$. Defining the confinement parameter β as $\beta = 2/(\kappa_i w_o)$, the lateral breakup will thus be prone to happen when $\beta > 1$, i.e., when:

$$\beta = 2 \frac{w_i/w_o}{1 + \frac{w_i}{h} + \sqrt{\left[\left(1 - \frac{w_i}{h}\right)^2 + \pi \frac{w_i}{h}\right]}} > 1. \quad (2)$$

We rearrange Eq. (2) and map in Fig. 2(c) the β value of a geometry as a function of its width ratio w_i/w_o and aspect ratio h/w_o , where the green to yellow region represents the geometrical conditions of $\beta > 1$ that should allow the corresponding T-junctions to produce lateral breakup. To test this criterion, we select eight T-junction geometries with different combinations of h/w_o and w_i/w_o on which droplet breakup experiments are conducted with varying Ca and initial droplet length $L(0)$ (normalized by inlet channel width w_i), see Table I. The outcomes of those experiments are represented as black (no lateral breakup) or red (with lateral breakup) markers in Fig. 2(c). No lateral breakup was observed for the two geometries with $\beta < 1$, while geometries that have $\beta > 1$ always showed lateral breakup for a given range of Ca and $L(0)$. It confirms that Eq. (2) is a good predictor for lateral breakup phenomenon on a T-junction. Note that a higher β value is always associated with a larger aspect ratio and/or a larger width ratio, shown in the contour map as markers that are further away from the diagonal. It suggests that the capillary instability leading to the lateral breakup

is driven by both of the two ratios. Indeed, the high aspect ratio ($h > w_o, h > w_i$) ensures that the confinement level on a droplet is dictated by the channel width (the smaller dimension). Then, the large width ratio ($w_i > w_o$) actually imposes the difference of confinement on the same droplet crossing the junction. Both conditions together create the necessary capillary pressure imbalance that eventually drives the lateral breakup.

C. Modelling the dynamics of the lateral breakup for lower Ca

Next, we derive a theoretical model to describe the dynamics of the lateral breakup, occurring in two steps. First, the droplet progresses through the channel until the necking criterion is met: This is the onset of the necking. Second, the necking-induced pocket of the continuous phase, fed via the gutters, inflates and thins down the droplet until the final pinch-off. The first step consists in finding the condition where a minimal value of $1/R_g^* = 2/w_o$ is met within the outlet channel. At an initial configuration, a droplet of dimensionless speed $Ca = \mu V/\gamma$ and an initial length $L(0)$ (not shown) passes the junction, creating gutters of length L_i and L_o in the inlet and outlet channel. We assume a homogeneous pressure p_d inside the droplet and decide to ignore potential surface-tension gradients induced by the elongation of surfactant-laden interfaces [53,54]. We obtain a hydraulic resistance per unit length:

$$r_h(s, t) = \frac{C\mu}{(1 - \pi/4)R_g(s, t)^4}, \quad (3)$$

where μ is the viscosity of the fluid, C is a geometric constant with $C = 93.93$ [52], and $R_g(s, t)$ is the radius of the gutter along the droplet internal coordinate s . Note that s is oriented along x in the inlet channel and along y in the right outlet channel. At the rear and front caps we have $R_g(0, t) = F_i$ and $R_g(L(t), t) = F_o$, where $F_{i,o} = \kappa_{i,o}^{-1}$ is the inverse of the total curvatures of the caps defined in Eq. (1). The quantity $L(t) = L_i(t) + L_o(t)$ designates the total length of the droplet (excluding caps) along s the internal abscissa. The difference between F_i and F_o induces a flow rate $q(t)$ of the continuous phase, allocated in gutters in the inlet channel and in 2×2 gutters in the outlet channels. Experimentally, we observed a reduction of droplet rear cap speed after the front cap enters the outlet channel [Fig. 3(a)], which confirms the presence of this total bypass flux $q(t)$. Combining the Young-Laplace equation for the pressure balance at the interface $p(s, t) = p_d - \gamma/R_g(s, t)$ and the Poiseuille equation expressing the pressure gradient within the continuous phase $\partial p/\partial s = -r_h q/4$, one obtains an equation controlling the shape of the gutters:

$$\frac{\partial R_g}{\partial s}(s, t) = -\frac{q(t)}{4\gamma} \frac{C\mu}{(1 - \pi/4) R_g(s, t)^2}, \quad (4)$$

with a continuous change of gutter radius $R_g(s, t)$ along the droplet from F_i to F_o . Solving Eq. (4) provides both $q(t)$ (constant in space due to flow rate conservation) and the gutter radius $R_g(s, t)$ at any location (s) along the droplet:

$$q(t) = \frac{(F_i^3 - F_o^3)}{AL(t)}, \quad \text{and} \quad (5)$$

$$R_g^3(s, t) = F_i^3 - q(t)As \quad \text{for} \quad 0 \leq s \leq L(t), \quad (6)$$

where $A = 3C\mu/[4\gamma(1 - \pi/4)]$. The total length of the droplet, $L(t)$, is found by imposing volume conservation from known initial droplet length $L(0)$ and $L_i(t)$. Specifically, the cross-sectional area being $S_g^{(i,o)} = hw_{i,o} - R_g^2(4 - \pi)$, the volume conservation

$$\int_{s=0}^{s=L_i(t)} S_g^{(i)} ds + \int_{s=L_i(t)}^{s=L(t)} S_g^{(o)} ds = \int_{s=0}^{s=L(0)} S_g^{(i)} ds$$

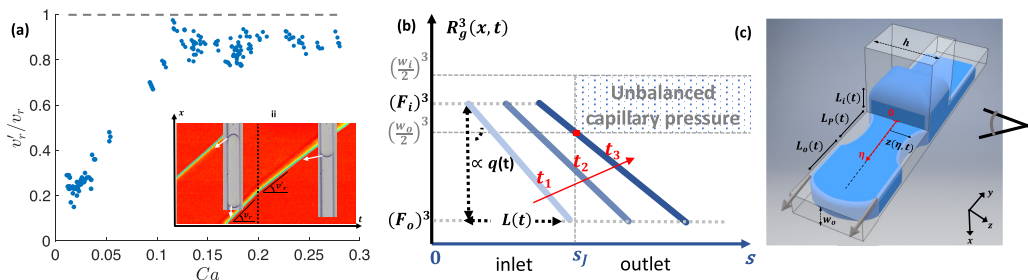


FIG. 3. (a) Relative rear cap velocity v'_r/v_r , once the droplet has entered the junction (see definition in the inset) versus the droplet capillary number Ca , for geometry A. Inset shows the kymograph from which droplet cap trajectory is measured (yellow line), whose slope before and after the vertical dotted line gives v_r and v'_r , respectively. (b) Result of step 1: Schematic plot of Eq. (6) using junction coordinate s . Each blue curve represents the cubic power of the gutter radius along the droplet, from F_i at the rear interface in the inlet to F_o at the front interface in the outlet. Three such gutter radius profiles are shown corresponding to three time points, i.e., three droplet locations, as the droplet advances inside the channel. At t_1 : the droplet is about to enter the junction; t_2 : part of the droplet passes the junction, but the gutter radius inside the outlet channel is below $R_g^* = w_o/2$; t_3 : the droplet further advances and $R_g = R_g^*$ is met at the red square; from this stage onward, further advancing will cause $R_g > R_g^*$ inside the outlet channel and onset of necking, and a pocket forms and inflates. (c) Modeling of step 2 (the pocket development for one arm of the T junction), with the eye showing the observation perspective during the experiment. During the inflation of the lateral pocket, the droplet can be divided into three regions with a length of $L_i(t)$, $L_p(t)$, and $L_o(t)$. The coordinate η starts from the junction and is parallel to the outlet channel. In the parts of length $L_i(t)$ and $L_o(t)$, gutters are maintained, and the gutter flows are represented by gray arrows.

is an implicit equation for $L(t)$. We then find the critical L_{ic} , such that $R_g = R_g^* = w_o/2$, by progressively decreasing L_i from $L(0)$ (the droplet turns the junction at $t = 0$), according to

$$L_i(t) = L(0) - \frac{v'_r}{v_r} t Ca,$$

where the empirical factor v'_r/v_r is a function of Ca , is shown in Fig. 3(b). Further advancing the droplet, $R_g > w_o/2$ cannot be met, and the necking has to start. The corresponding critical time t_c can be obtained from $L_{ic} = L(0) - Cat_c$. Figure 3(b) plots R_g^3 , changing linearly from F_i^3 to F_o^3 along the droplet, for three timestamps and corresponding droplet locations during the advancing of the droplet. It illustrates the following scenario for the onset of the necking: With the droplet advancing in the channel, the rear cap approaches the junction and increases more and more the gutter radius in the outlet channel, which eventually goes beyond the maximum possible value fixed by the outlet channel geometry, thus falling out of balance. Such a process is strongly influenced by the flow rate and droplet size, which change the slope and length of the R_g^3 curve. As the maximum gutter radius along the outlet channel is always attained at the junction location (s_j), it is always at the junction that the necking requirement is first met. Thus, the pocket of continuous phase is expected to start forming from the junction, which is confirmed by the experiment, as discussed below.

Now the droplet enters a second phase consisting in the development of the pocket. To model the evolution of such process, we divide the droplet into three consecutive parts [Fig. 3(c)]: the part in the inlet channel of length $L_i(t)$ with gutters and the part on the spatial interval of $0 \leq \eta \leq L_p$, where $L_p(t)$ is the length of the pocket, from the junction ($\eta = 0$) to where the droplet curvature in the direction of the flow vanishes [$\eta = L_p(t)$]. The third part corresponds to the remaining of the droplet in the outlet channels where the gutter is resumed, of length $L_o(t)$. In the pocket region, we parametrize the droplet surface by its curvature in the flow direction [i.e., the curvature in the y - z

plane in Fig. 3(a)], defined as

$$k(\eta, t) = -\frac{\partial}{\partial \eta} \left[\frac{\partial z(\eta, t)/\partial \eta}{\sqrt{1 + (\partial z(\eta, t)/\partial \eta)^2}} \right], \quad (7)$$

where $z \in [w_o/2; h/2]$ designates the interfacial position: z equals $h/2$ when no pocket is formed and gutters are maintained, and $z = w_o/2$ corresponds to a cylindrical droplet cross section that represents the end point of the pocket development. The curvature in the direction perpendicular to the flow, i.e., the curvature in the x - z plane in Fig. 3(a), is assumed constant and equals $2/w_o$, such that the total curvature of the droplet in the pocket region writes $k(\eta, t) + 2/w_o$. We then define the continuity equation for the continuous phase as $\partial S/\partial t = (\partial q/\partial \eta)/2$, where $S[z(\eta, t)] = (\pi - 4)w_o^2/4 + 2z(\eta, t)w_o$ is the cross-sectional area of the discrete phase in one outlet channel, which is fed by two quarter-sections at the top wall with a flow rate of $q(\eta, t)/4$ in each. We apply the derivative with respect to η to the equation of the pressure balance at the interface to obtain the flow rate

$$q(\eta, t) = \frac{4\gamma}{r_{h,s}[z(\eta, t)]} \frac{\partial k(\eta, t)}{\partial \eta}, \quad (8)$$

where $r_{h,s}[z(\eta, t)]$ designates the hydrodynamic resistance per unit length of a quarter-section, which reduces to Eq. (3) for $z = h/2$. Injecting both the expression for $S[z(\eta, t)]$ and Eq. (8) in the continuity equation leads to

$$\frac{\partial z(\eta, t)}{\partial t} = \frac{\gamma}{w_o} \frac{\partial}{\partial \eta} \left\{ \frac{1}{r_{h,s}[z(\eta, t)]} \frac{\partial k(\eta, t)}{\partial \eta} \right\}, \quad (9)$$

such that Eq. (7) and Eq. (9) constitute a system of two coupled equations for the two unknowns $z(\eta, t)$ and $k(\eta, t)$. It is subject to two boundary conditions for z : $z(0, t) = z(L_p(t), t) = h/2$, as well as two for k : $k(0, t) = \kappa_J - 2/w_o$, and $k(L_p(t), t) = 0$, where κ_J is the curvature of the inlet gutter at the junction, found by matching with the inlet gutter regime (see Appendix). As mentioned, the necking condition has already been met, thus $k(0, t) \leq 0$, resulting in the opening of the pocket; however, $k(\eta, t)$ must increase with η until recovering $k(L_p(t), t) = 0$, as the hydrodynamic resistance induces a pressure drop of the continuous phase [see Eq. (8)]. We used a finite-element method to calculate the dynamics of the necking process numerically, i.e., $z(\eta, t)$ and $k(\eta, t)$. The boundary conditions, numerical discretization and nondimensionalization used for this purpose are detailed in the Appendix and numerical methods section. The result of the simulation resolves the pocket evolution process, which can be represented by the change of pocket length $L_p(t)$ and depth $z(\eta, t)$. We modeled the event presented in Fig 2(b) (blue) and compared the theoretical predictions with experimental observations in Fig. 4. In Fig. 4(a) we show the dynamics of a droplet advancing in the inlet channel by means of a kymograph (increasing time in the y axis), where the color is correlated to the light intensity received by the camera, which gives a hint on the droplet topography during the process. In Fig. 4(b) the left panel is the kymograph of the same droplet during the same event but only shows the front caps advancing in the outlet channel; the right panel displays with the same spatial and temporal scales the corresponding dynamics as predicted by the model. In the model, the shades of gray and the isocontours stand for the normalized interface position $z(\eta, t)/h$. The distance between the symmetry axis and the solid black line is the predicted length of the droplet in the outlet channel. At $z(\eta, t) = w_o/2$, a locally cylindrical cross section is reached which is considered as the trigger of a fast breakup controlled by surface tension. We thus consider this moment as the theoretical breakup time point. The parameters of Ca , $L(0)$, and v_r/v_r for simulation are extracted from the experiment in comparison.

The linear increase of the droplet length is well captured by the model. However, the pocket inflation rate is overestimated by the model, in particular after the rear cap of the drop arrives at the junction and undergoes changes of curvature. The model suggests the following scenario for the lateral breakup: After the rear of the droplet reaches the corner (and the volume of the

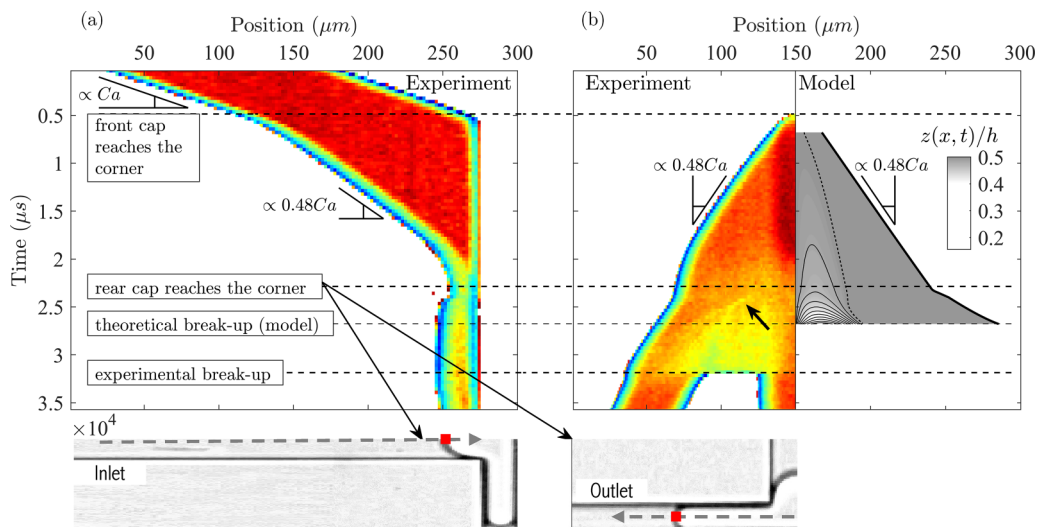


FIG. 4. Temporal evolution of the part of the droplet (a) in the inlet channel and (b) in the outlet channels. For (b) the experimental kymograph (on the left) is compared with the model predictions (on the right). Four horizontal dashed lines are drawn at successive time points where (i) the front of the droplet reaches the entry point of the lateral channels, (ii) the rear of the droplet reaches the same point, (iii) the breakup of the droplet is predicted by the model, and (iv) the droplet breakup is observed experimentally. At the time when the rear of the droplet reaches the corner, a bright field image of the droplet in the channel is shown at the bottom of (a) and (b) oriented accordingly, where the gray dashed arrows indicate the advancing direction of the droplet caps (red) with time. The scale of these images corresponds exactly to the spatial scale of the kymographs. The proportionality sign (\propto) in the indications of the slopes implies a change of units, necessary to obtain a nondimensional slope. The geometry is $w_o/h = 14/37$, $w_i/h = 30/37$ (geometry B), the initial droplet length $L(0)/w_i = 2.8$, and the capillary number $Ca = 0.01$.

rear cap reaches a stationary regime), a gutter flow of flow rate $Ca w_i h$ enters the pocket, which is thus inflating while decreasing its resistance; as the pocket is less and less resistive, it is more and more favorable for the flow to accumulate inside instead of bypassing through the outlet gutter (comparatively much more resistive). This process self-amplifies, the consequence of which the pocket localizes and deepens very fast after the rear of the droplet has reached the corner [see the dense contour line, i.e., the fast hollowing after the “rear cap reaches the corner” time point in Fig. 4(b)]. However, the experimental data suggest that the dynamics of pocket inflation are overestimated by the model. The black arrow in the experimental kymograph [Fig. 4(b), left panel] highlights the onset of a downstream propagation of what we believe to be the location of the pocket interface. Indeed, from that time the pocket is sufficiently deep to be observable on the kymograph, but as we mentioned the pocket is thought to exist even earlier. The fast propagation of the pocket interface, faster than the increase rate of the droplet length, seems to indicate that the pocket spreads along the entire length of the droplet in the outlet channel. Thereby, unlike in the model, the incoming flow rate is not subject to a fast accumulation in a localized low-resistance region, and thus the breakup occurs later and further downstream. This fact might also imply a dependency on the initial length of the droplet. A possible reason for the relative inaccuracy of the model is the large value of the experimental capillary number Ca . In fact, the domain of validity of the model is restricted to low Ca for two main reasons. First, increasing values of Ca may lead to a cross-section occupancy of both liquids which is not accounted for in our gutter model. This was first computed analytically in Ref. [55] in the asymptotic limit of small Ca , where the lubrication film around the droplet, say, δ , was shown to increase as $\delta \sim Ca^{2/3}$; therefore, the values of the rear and front caps curvatures $\kappa_{i,o}$ needs to be computed on $h - 2\delta$ and $w_{i/o} - 2\delta$ in (1), thus

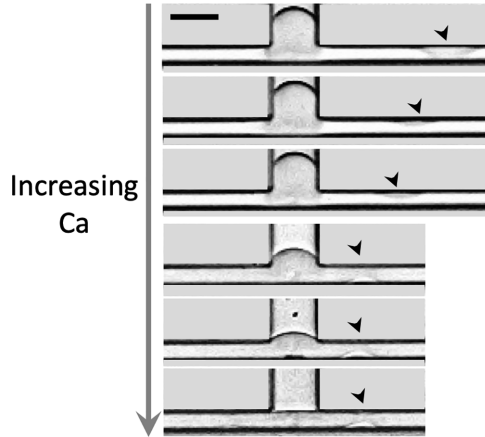


FIG. 5. Breakup moment of six breakup events with increasing Ca . The Ca value from top to bottom is 0.016, 0.025, 0.056, 0.088, 0.129, and 0.177. The breakup location in the right outlet channel is shown with black arrowheads. The scale bar represents $30\ \mu\text{m}$.

modifying all ensuing geometrical quantities. In Ref. [56], this modification was shown to have a significant impact on the value of the droplet volume (which incorporates the caps and the gutter curvatures) from $Ca \approx 10^{-3}$ (see their Fig. 7). The work of De Lozar *et al.* [57,58] experimentally and numerically (respectively) generalize the description of the flow above the asymptotic limit of small Ca . For the aspect ratios of the inlet and outlet channels considered in the present paper, Fig. 3 in Ref. [57] also suggests the cross-section occupancy of the continuous phase to significantly increase after $Ca \approx 10^{-3}$, at least for a discrete phase of zero viscosity as considered in Ref. [57]. The second reason for the model to lose accuracy for large Ca is the increasing contribution of the viscous dissipation. For a given geometry, the associated pressure drop has been shown to increase linearly with the droplet capillary number [23,59,60] and thus needs to be accounted for when Ca is large, which was not done in the model. For all these reasons, we estimate the model to be *a priori* valid up to $Ca \approx 10^{-3}$. Experimentally, we observed an evolution of lateral breakup behavior from low to high Ca condition. For lower Ca , a pocket forming process starts and stops before the rear interface reaches the junction. The corresponding breakup distance from the junction decreases with increasing Ca (Fig. 5). For higher Ca , the breakup location is stabilized, and a decreasing rear cap curvature is observed as Ca increases (Fig. 5). We next discuss the latter case concerning higher Ca .

D. A central breakup recovered at higher Ca

At higher Ca , when a critical value Ca^* is exceeded, the conventional central breakup is recovered, even for geometries enabling lateral breakup. Figure 6(a) shows three breakup events with the same droplet size. Central breakup is observed at higher values of Ca , while both lateral and central breakups can occur simultaneously near the critical value Ca^* . In Fig. 6(b) we show light intensity kymographs of two breakup events with the same droplet size but different breakup regimes. The existence of the lateral pocket can be detected by a faint intensity change, caused by the light scattering at the openings. First, it confirms that the necking starts from the junction as predicted by our model [Fig. 3(c)]. Second, it is remarkable that the pocket formation occurs regardless of the final breakup outcome. This observation, together with the coexistence of lateral and central breakups near the critical Ca^* indicates that the two processes are simultaneous. It gives a hint on the breakup transition mechanism, attributed to the faster completion of central breakup that aborts the lateral breakup process.

In Fig. 6(c), we plot the regime map near the transition zone for Ca_o versus \bar{L}_o . Here $Ca_o = Ca(w_i/w_o)/2$ is the outlet channel capillary number, and $\bar{L}_o = L(0)(w_i/w_o)/w_o/2$ is the initial

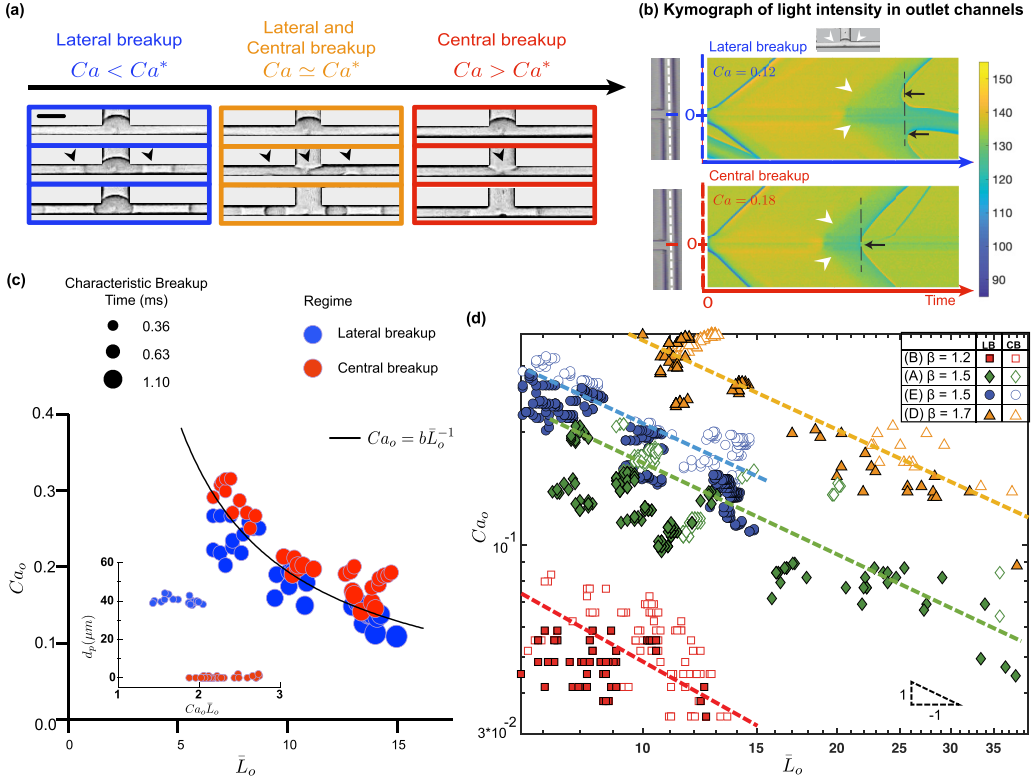


FIG. 6. (a) Time sequences of example breakup events for the same droplet length under three flow conditions. The breakup regime shifts from lateral to central breakup from low to high Ca . The scale bar represents $30 \mu\text{m}$. (b) Kymograph of light intensity along the central part of the outlet channel (white dashed line) for two droplets of the same size but with different regimes; The gray value is turned into colors in the colormap. At time zero, both droplets enter the junction, the trajectory of the front interface forms a straight line. After the rear interface arrives at the junction (inset), the change of intensity due to the light scattering from the interface of the pocket is captured (white arrowheads), which always starts from the junction as predicted. At the end of each process, new interface(s) is formed at the locations indicated by the black arrows. (c) The breakup transition regime map of Ca_o versus \bar{L}_o for geometry A [Fig. 2(c)], where $Ca_o = Ca(w_i/w_o)/2$ and $\bar{L}_o = L(0)(w_i/w_o)/w_o/2$. Blue and red circles represent lateral and central breakups, respectively. The area of each circle is proportional to the characteristic breakup time, defined from when droplet rear interface reaches the junction to the final breakup moment. The black curve represents the function $Ca_o = b\bar{L}_o^{-1}$, where $b = 1.9$ in this case (geometry A). Inset: d_p , the pinch off lateral distance from the junction center (in μm) versus the product of $Ca_o\bar{L}_o$. (d) Logarithmic representation of the breakup transition regime map for Ca_o vs. \bar{L}_o for four geometries (A, B, D, and E) with different β values, represented by four colors. The filled and hollow markers represent lateral (LB) and central breakups (CB), respectively. Dashed lines of slope -1 are represented to guide the eyes.

droplet length translated into outlet channel (divided by 2 for only one branch) normalized by the outlet width. We compare the characteristic breakup time for both regimes, defined as the duration from the rear cap reaching the corner until the breakup and represented in Fig. 6(c) as the surface area of the round markers. Interestingly, the characteristic time decreases approximately with increasing Ca for both regimes. But at each transition point the central breakup always has a shorter characteristic time than the adjacent lateral breakup.

Concerning length dependency, longer droplets need a lower critical Ca_o^* for a central breakup to occur. We found that the regime transition can be well adjusted by the inverse power law

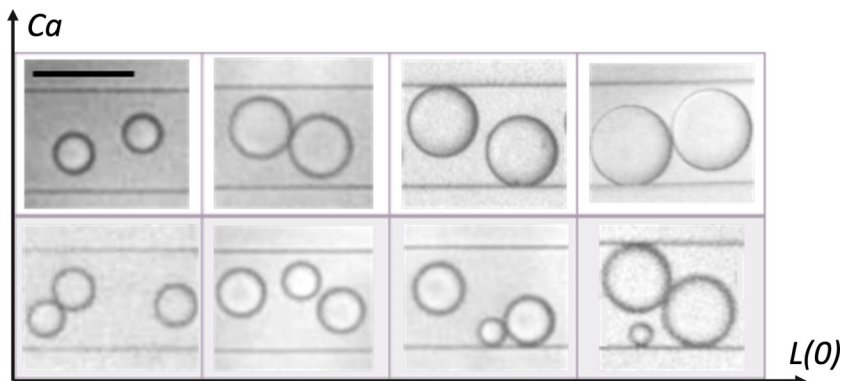


FIG. 7. Different daughter droplet composition from each droplet breakup event, with geometry B. From top to bottom: increasing the number of daughter droplets (by decreasing the capillary number Ca). From left to right: increasing the daughter droplet size and/or size ratio [by increasing the droplet length $L(0)$]. The scale bar represents $100 \mu\text{m}$.

$Ca_o^* \sim b\bar{L}_o^{-1}$. This leads to a critical constant $(Ca_o\bar{L}_o)^*$ that solely governs the lateral/central breakup transition. In the inset of Fig. 6(c), the separation of the two regimes by $(Ca_o\bar{L}_o)^* \approx 1.9$ is shown. Remarkably, an inverse power law also characterizes the nonbreakup/central breakup transition in conventional T-junctions for long droplets, as shown by Haringa *et al.* [44]. However, the prefactor 1.9 obtained in our geometry is much higher (by orders of magnitude) than the values obtained in conventional T-junctions, as reported by Haringa *et al.* [44] (see the Appendix for more detailed comparisons). This huge difference in prefactors sheds light on the main difference between conventional T-junctions and the novel geometries presented in our studies: the hydrodynamic resistance of the gutters. In our novel T-junctions geometries, the continuous flow of the carrier fluid arriving at the junction may follow three different paths: (a) bypassing the entire droplet through gutters, (b) flowing into the lateral pockets and increase their volume, or (c) pushing the rear cap and contributing to central breakup. However, in conventional T-junctions, there is no lateral pocket to inflate. Furthermore, gutters are much narrower and resistive, precisely due to the absence of lateral pockets [44]. These major differences explain why central breakup is more prone to happen in conventional T-junctions, thereby explaining the much smaller prefactors reported in the literature compared to the ones obtained in our nonconventional T-junctions. In Fig. 6(d), the result for four different geometries are presented (geometries A, B, D, and E in the table). For all the tested geometries, Ca_o^* is proportional to the inverse of \bar{L}_o , similarly to the above observation but with prefactors varying among the geometries. Remarkably, geometries with more prominent lateral breakup (higher value of β) require a higher Ca_o^* to recover central breakup.

In a nutshell, the droplet breakup fate in these novel T-junctions should be determined by the temporal dynamics of both breakup processes and is dominated by the faster one. Our analysis could not quantitatively capture the competition between those two ongoing processes. In particular, the incessant structural changes of the gutters and the lateral pockets question the relevance of a derivation considering droplets at equilibrium, which constrats with what is possible in conventional T-junctions. In terms of application, note that by merely shifting flow condition, the droplet size and/or composition can be changed on-fly (Fig. 7), which opens interesting perspectives for the field of droplet microfluidics [61].

IV. CONCLUSION AND OUTLOOK

In summary, we reported on a novel lateral droplet breakup occurring in microfluidic T-junctions which leads to the formation of three daughter droplets. We experimentally evidenced that this new

regime arises from an unbalanced capillary pressure at the droplet interface induced by the strong gradient of confinement across the junction (provided that $h > w_i > w_o$). A geometrical design rule was proposed accordingly to enable the lateral breakup regime. We also developed a model depicting the development of the lateral pockets responsible for the ultimate lateral breakup for low capillary number Ca . Furthermore, we showed that a unique central breakup is recovered at higher Ca , a mechanism also observed in conventional T-junctions. We showed that the critical capillary number Ca^* marking this transition from lateral to central breakup is compatible with an inverse dependency on the droplet length. The presence of the lateral pockets and their inflation explains that the values of Ca^* are orders of magnitude higher than the prediction in the presence of highly resistive gutters, a strong difference with what is observed in conventional T-junctions where no lateral pocket is present [44]. Accounting for a thickening of the gutter at higher Ca , as observed by Lozar *et al.* [57], was not sufficient to explain the high values of Ca^* reported (not shown).

The analysis of Leshanski *et al.* [42] in square cross-section T-junctions considered the inflation and opening of a central pocket in order to interpret the transition from drop splitting to intermittent blockage regime. The authors showed, by comparison with 2D interface-resolving direct numerical simulations and three-dimensional experiments with square cross sections, that the subtle combination of volume flux conservation and a Tanner-like law for the progression of the leading edge of the pocket are sufficient to precisely model this phenomenon. The Tanner-like law models the action of the lubrication forces in the dynamical meniscus region bridging the pocket region to the thin film region. Such excellent agreement was obtained neglecting gutter flows. However, given the pronounced three-dimensional nature of the T-junction geometries used in our study and the capillary number range investigated, which reinforces the importance of gutter flows, we have not been capable to build a lumped description of the dynamic meniscus region connecting the lateral pockets to the flat film region, the gutter flows, and the pocket inflation rate. Furthermore, the simultaneous inflation of the two lateral pockets and of the central pocket renders volume conservation assumptions difficult to use efficiently, as opposed to T-junctions with square cross sections [42,44] where a unique central pocket grows. A thorough theoretical determination of Ca^* remains to be achieved and is a challenge for future studies due to the constant changes of shape underwent by the gutters and the lateral pockets during the penetration of the droplet in the junction.

A remarkable feature of the T-junction geometry we explored is that both hydrodynamic-stress-driven and surface-tension-driven mechanisms are enabled simultaneously, which allows new microfluidics functionalities. On one hand, active control over the flow condition can change droplet composition and sizes without changing geometries. On the other hand, without active control, the mere change of the content or property of the droplet can alter the competition of the two breakup regimes thus shifting the breakup results for passive applications as shown in a recent study [61] where the presence or absence of particle in a drop could trigger one breakup mode or the other. Altogether, we expect that our study will provide new versatile tools to the community to manipulate and control the volume of droplets.

ACKNOWLEDGMENTS

This work was supported by the Swiss National Science Foundation (Grant No. 200341). The authors also thank Personalized Health and Related Technologies (PHRT), a strategic focus area of the Swiss ETH Domain for financial support.

APPENDIX A: MATHEMATICAL MODELING OF THE INFLATION OF THE LATERAL POCKETS AT LOW Ca

Here after, we fully characterize the inlet and outlet gutters regime of the droplet [shown in Fig. 3(a)], as they couple with Eqs. (7) and (9) for the pocket dynamic through the boundary conditions and the conservation of the droplet volume. We then show that they constitute all together

a closed system that is made nondimensional and, after some mathematical rearrangements, can be directly integrated in time.

Let $R_g^{(i)}(s, t)$ designate the radius of the gutter in the inlet channel [see Fig. 3(a)] whose internal coordinate is $s \in [0; L_i(t)]$, purely along the x direction. Solving Eq. (4) subject to $R_g^{(i)}(0, t) = F_i$ leads to

$$R_g^{(i)}(s, t)^3 = F_i^3 - q_i(t)As, \quad (\text{A1})$$

where $q_i(t)$ is the inlet gutter flow rate. By continuity, we can express it in terms of $k(\eta, t)$ using Eq. (8) as

$$q_i(t) = \frac{4\gamma}{r_{h,s}[z(0, t) = h/2]} \frac{\partial k(0, t)}{\partial \eta}, \quad (\text{A2})$$

[we recall that $\eta = 0$ designates the opening of the pocket at the junction and $\eta = L_p(t)$ its closure; see Fig. 3(a)]. The four boundary conditions for $z(\eta, t)$ and $k(\eta, t)$ write $z(0, t) = z(L_p(t), t) = h/2$, $k(0, t) = 1/R_g^{(i)}(L_i(t), t) - 2/w_o$, and $k(L_p(t), t) = 0$. The outlet gutter, of length $L_o(t)$ [see Fig. 3(a)], has a radius $R_g^{(o)}(\alpha, t)$ whose internal coordinate is $\alpha \in [0; L_o(t)]$, purely along the y direction. The radius $R_g^{(o)}(\alpha, t)$ is characterized by solving Eq. (4) subject to $R_g^{(o)}(0, t) = w_o/2$ [since $k(L_p(t), 0) = 0$]:

$$R_g^{(o)}(\alpha, t)^3 = \left(\frac{w_o}{2}\right)^3 - q_o(t)A\alpha, \quad \text{where} \quad q_o(t) = \frac{4\gamma}{r_{h,s}[z(L_p(t), t) = h/2]} \frac{\partial k(L_p(t), t)}{\partial \eta}. \quad (\text{A3})$$

Its length $L_o(t)$ is easily determined by imposing $R_g^{(o)}(L_o(t), t) = F_o$. As will become clear in a moment, the problem is closed by imposing of conservation of the total volume of the droplet. From now on quantities are made nondimensional by h in space and $\mu h/\gamma$ in time,

$$\begin{aligned} h(\tilde{s}, \tilde{\eta}, \tilde{\alpha}) &= (s, \eta, \alpha), & \frac{\mu h}{\gamma} \tilde{t} &= t, & h^2 \tilde{S} &= S, & \frac{h^2 \gamma}{\mu} \tilde{q} &= q, & \frac{1}{h} \tilde{k} &= k, & h \tilde{z} &= z, \\ \frac{\mu}{h^4} \tilde{r}_{h,s} &= r_{h,s}, & \text{and} & & \frac{\gamma}{\mu} \text{Ca} &= U. \end{aligned}$$

Equations (7) and (9) thus are nondimensionalized, and they are then put in the form of a classical conservation law for $\tilde{z}(\tilde{\eta}, \tilde{t})$ and $\tilde{k}(\tilde{\eta}, \tilde{t})$:

$$\begin{bmatrix} 1 & 0 \\ 0 & 0 \end{bmatrix} \frac{\partial}{\partial \tilde{t}} \begin{bmatrix} \tilde{z} \\ \tilde{k} \end{bmatrix} + \frac{\partial}{\partial \tilde{\eta}} \left[-B \frac{1}{r_{h,s}[\tilde{z}]} \frac{\partial \tilde{k}}{\partial \tilde{\eta}} \right] = \begin{bmatrix} 0 \\ \tilde{k} \end{bmatrix}, \quad \text{for} \quad 0 \leq \tilde{\eta} \leq L_p(\tilde{t}), \quad (\text{A4})$$

where all the tildes have been dropped and $B = 1/w_o$ is a constant (it is understood that L_p and w_o have been made nondimensional by h , etc.). System (A4) is rewritten under the change of variable $\xi = \eta/L_p(t)$ in order to be solved over the time-independent domain $0 \leq \xi \leq 1$, which is significantly more convenient. The partial derivatives are transformed as $\partial_t \rightarrow \partial_t - (d_t L_p) L_p^{-1} \xi \partial_\xi$ and $\partial_\eta \rightarrow L_p^{-1} \partial_\xi$:

$$\begin{bmatrix} 1 & 0 \\ 0 & 0 \end{bmatrix} \frac{\partial}{\partial t} \begin{bmatrix} \tilde{z} \\ \tilde{k} \end{bmatrix} + \frac{\partial}{\partial \xi} \left[-\frac{dL_p}{dt} \frac{1}{L_p} \xi \tilde{z} - \frac{B}{L_p^2} \frac{1}{r_{h,s}[\tilde{z}]} \frac{\partial \tilde{k}}{\partial \xi} \right] = \begin{bmatrix} -\frac{dL_p}{dt} \frac{1}{L_p} \tilde{z} \\ \tilde{k} \end{bmatrix}, \quad (\text{A5})$$

where $z(\eta, t) = \tilde{z}(\xi, t)$ and then $k(\eta, t) = \tilde{k}(\xi, t)$. Under this change of variables the flow rate $q(\eta, t) = \tilde{q}(\xi, t)$ occurring inside the pocket, and the flow rates $q_i(t)$ and $q_o(t)$ occurring inside

the inlet and outlet gutters, respectively, express:

$$\bar{q}(\xi, t) = \frac{4}{r_{h,s}[\bar{z}(\xi, t)]L_p(t)} \frac{\partial \bar{k}}{\partial \xi}(\xi, t), \quad q_i(t) = \bar{q}(0, t), \quad \text{and} \quad q_o(t) = \bar{q}(1, t).$$

The boundary conditions of system (A5) are rewritten:

$$\begin{aligned} \bar{z}(0, t) &= 1/2, \quad \bar{z}(1, t) = 1/2, \\ \bar{k}(0, t) &= \left\{ [F_i^3 - q_i(t)AL_i(t)]^{-1/3} - \frac{2}{w_o} \right\}, \quad \text{and} \quad \bar{k}(1, t) = 0. \end{aligned} \quad (\text{A6})$$

[with the nondimensional $A = 3C/(4 - \pi)$]. A third equation is necessary for the third unknown $L_p(t)$, and the problem is closed by imposing the volume conservation $V(t) = V(0)$. Let $V_g^{(i)}(t)$ designate the volume of the part of the droplet contained in the inlet channel and where a gutter is present [i.e., for $0 \leq s \leq L_i(t)$]; the volume of the rear cap is in addition $V_{\text{cap}}^{(i)}(t)$. Accordingly, let $V_g^{(o)}(t)$ be the volume of the part of the droplet contained in one of the two outlet channels and where a gutter is present [i.e., for $0 \leq \alpha \leq L_o(t)$]; the volume of one front cap is in addition $V_{\text{cap}}^{(o)}$. We recall that the expression for the cross-sectional area of the discrete phase in the pocket region is $S[z(\eta, t)] = (\pi - 4)w_o^2/4 + 2w_o z(\eta, t)$, such that it is associated to a volume contribution in a outlet channel of $\int_0^{\eta=L_p(t)} S[z(\eta, t)]d\eta$. Eventually,

$$\begin{aligned} V(t) &= 2V_{\text{cap}}^{(o)} + V_{\text{cap}}^{(i)}(t) + V_g^{(i)}(t) + 2V_g^{(o)}(t) + 2 \int_0^{\eta=L_p(t)} S[z(\eta, t)]d\eta \\ &= 2V_{\text{cap}}^{(o)} + V_{\text{cap}}^{(i)}(t) + V_g^{(i)}(t) + 2V_g^{(o)}(t) + 2L_p(t) \left[\frac{(\pi - 4)w_o^2}{4} + 2w_o \int_0^{\xi=1} \bar{z}(\xi, t)d\xi \right] = V(0). \end{aligned} \quad (\text{A7})$$

In addition, the cross-sectional area the drop in a region where a gutter (of radius R_g) is present is $S_g^{(i,o)} = hw_{i,o} - [R_g^{(i,o)}]^2(4 - \pi)$, such that

$$V_g^{(o)}(t) = \int_{\alpha=0}^{\alpha=L_o(t)} S_g^{(o)}(\alpha, t)d\alpha = \frac{1}{Aq_o(t)} \left\{ hw_o \left[\left(\frac{w_o}{2} \right)^3 - F_o^3 \right] - \frac{3(4 - \pi)}{5} \left[\left(\frac{w_o}{2} \right)^5 - F_o^5 \right] \right\},$$

and we compute similarly

$$V_g^{(i)}(t) = hw_i L_i(t) - \frac{3(4 - \pi)}{5Aq_i(t)} \{ F_i^5 - [F_i^3 - L_i(t)Aq_i(t)]^{5/3} \}.$$

In order to mimic a constant-velocity progression of the droplet in the inlet channel before the rear droplet interface reaches the junction, as observed experimentally, the length $L_i(t)$ is chosen as a ramp in time

$$L_i(t) = \begin{cases} L_i(0) - \frac{v'_r}{v_r} \cdot t \cdot \text{Ca} & \text{if } 0 \leq t \leq t_J \\ 0 & \text{if } t \geq t_J \end{cases}, \quad (\text{A8})$$

which acts as a source of excitation for the system (A5) trough the boundary condition for $\bar{k}(0, t)$ in (A6). At the time $t_J = L_i(0)/(\frac{v'_r}{v_r} \text{Ca})$ the rear droplet interface reaches the junction, and $L_i(0)$ is such that the necking condition as shown in Fig. 3(c) is met. The coefficient $\frac{v'_r}{v_r}$ multiplying Ca arises from the experimental data [shown in Fig. 3(b)]. The rear cap volume and curvature need also to be treated differently depending on whether t is smaller or larger than t_J ; let $V_{\text{cap}}[h, w_i]$ designate the equilibrium volume of the rear cap, whose value is taken from Musterd *et al.* [56] for $H/W \leq 1$,

$$A_{bd}[H, W] = HW - 4 \cdot F[W, H]^2(1 - \pi/4) = HW + F[W, H]^2(\pi - 4)$$

$$L_{\text{cap}}[H, W] = \frac{W}{2}$$

$$V_{\text{cap}}[H, W] = \int_0^{L_{\text{cap}}} A_{bd}[H, W] \left(1 - \frac{y^2}{L_{\text{cap}}[H, W]^2}\right) dy = \frac{2}{3} L_{\text{cap}}[H, W] A_{bd}[H, W].$$

Thereby the rear cap volume $V_i^{\text{cap}}(t)$ is implemented as

$$V_i^{\text{cap}}(t) = \begin{cases} V_{\text{cap}}[h, w_i] = cst & \text{if } 0 \leq t \leq t_J \\ V_{\text{cap}}[h, w_i] \frac{\mathcal{C}_i(t)}{\kappa_i} & \text{if } t \geq t_J \end{cases}, \quad (\text{A9})$$

where $\mathcal{C}_i(t)$ is the rear cap curvature with $\mathcal{C}_i(t \leq t_J) = \kappa_i$. Above $t = t_J$, the rear droplet interface must undergo the incoming flow rate $hw_i\text{Ca}$ and the following equation for the cap volume is activated:

$$\frac{dV_i^{\text{cap}}}{dt} = q_i(t) - \text{Ca} hw_i. \quad (\text{A10})$$

Injecting (A9) into (A10) leads to an evolution equation for $\mathcal{C}_i(t)$ for $t \geq t_J$, and the boundary condition for the curvature at the opening of the pocket is accordingly replaced by $k(0, t) = \mathcal{C}_i(t) - 2/w_o$ for these times.

APPENDIX B: A SCALING ARGUMENT FOR ONSET OF CENTRAL BREAKUP

We here demonstrate that the presence of lateral pockets induced by the confinement gradient dramatically changes the critical capillary number leading to central breakup, compared to conventional T-junctions with no confinement gradient. In the spirit of the work of Haringa *et al.* in conventional T-junctions [44], we derive an estimate of the critical capillary number for central breakup to happen in the fictitious case where no lateral pocket is present and where the carrier fluid has to bypass the droplet in highly resistive gutters. Note that this hypothesis is valid in conventional T-junctions, which led to experimentally validated theoretical predictions [44]. With this hypothesis, the inversely proportional relationship between Ca^* and L_o/w_o may be understood as follows: Once the body of the droplet has fully entered the outlet channels, we consider a threshold situation where the rear cap is flat for the observer, such that the rear cap curvature is assumed $1/F_i = 2/h$, although the precise value of the latter has little influence on the scaling law derived hereafter. The threshold capillary number above which a central breakup is expected is obtained by balancing the continuous flow rate arriving in the junction ($\text{Ca}w_i h$), with the capillary flow rate in the four gutters located in the outlet channel [$4(1/F_o - 2/h)/(r_o L_o)$], the quantity r_o being the hydraulic resistance per unit length of a gutter in the outlet channel. This leads to:

$$\frac{w_o}{w_i} \text{Ca}^* \sim \frac{4w_o}{w_i^2 h r_o L_o} \left(\frac{1}{F_o} - \frac{2}{h}\right) \propto \left(\frac{L_o}{w_o}\right)^{-1}. \quad (\text{B1})$$

In our geometry, for $w_o = 14/62$, $w_i = 30/62$, $h = 1$ and using Eq. (1) for F_o and Eq. (3) with $R_g = w_o/2$ for r_o , we obtain $4(\frac{1}{F_o} - \frac{2}{h})/(w_i^2 h r_o) \approx 5 \times 10^{-5}$. However, this corresponds to a value of $w_o/w_i \text{Ca}^*$ approximately four orders of magnitude smaller than experimental values. This major difference proves that it is impossible to neglect the contribution of lateral pockets, which massively decrease the hydrodynamic resistance of the gutters in our nonconventional T-junction geometry.

-
- [1] L. Shang, Y. Cheng, and Y. Zhao, Emerging droplet microfluidics, *Chem. Rev.* **117**, 7964 (2017).
 [2] P. Zhu and L. Wang, Passive and active droplet generation with microfluidics: A review, *Lab Chip* **17**, 34 (2017).
 [3] M. Joanicot and A. Ajdari, Droplet control for microfluidics, *Science* **309**, 887 (2005).

- [4] A. C. Sun, D. J. Steyer, A. R. Allen, E. M. Payne, R. T. Kennedy, and C. R. Stephenson, A droplet microfluidic platform for high-throughput photochemical reaction discovery, *Nat. Commun.* **11**, 6202 (2020).
- [5] Z. Swank, G. Michielin, H. M. Yip, P. Cohen, D. O. Andrey, N. Vuilleumier, L. Kaiser, I. Eckerle, B. Meyer, and S. J. Maerkl, A high-throughput microfluidic nanoimmunoassay for detecting anti-sars-cov-2 antibodies in serum or ultralow-volume blood samples, *Proc. Natl. Acad. Sci. USA* **118**, e2025289118(2021).
- [6] Y. Wang, R. Jin, B. Shen, N. Li, H. Zhou, W. Wang, Y. Zhao, M. Huang, P. Fang, S. Wang *et al.*, High-throughput functional screening for next-generation cancer immunotherapy using droplet-based microfluidics, *Sci. Adv.* **7**, eabe3839 (2021).
- [7] A. Kulesa, J. Kehe, J. E. Hurtado, P. Tawde, and P. C. Blainey, Combinatorial drug discovery in nanoliter droplets, *Proc. Natl. Acad. Sci. USA* **115**, 6685 (2018).
- [8] B. Schuster, M. Junkin, S. S. Kashaf, I. Romero-Calvo, K. Kirby, J. Matthews, C. R. Weber, A. Rzhetsky, K. P. White, and S. Tay, Automated microfluidic platform for dynamic and combinatorial drug screening of tumor organoids, *Nat. Commun.* **11**, 5271 (2020).
- [9] N. G. Durmus, S. Tasoglu, and U. Demirci, Functional droplet networks, *Nat. Mater.* **12**, 478 (2013).
- [10] Y. Zhang, Z. Dong, C. Li, H. Du, N. X. Fang, L. Wu, and Y. Song, Continuous 3d printing from one single droplet, *Nat. Commun.* **11**, 4685 (2020).
- [11] R. K. Kumar, T. A. Meiller-Legrand, A. Alcinesio, D. Gonzalez, D. A. Mavridou, O. J. Meacock, W. P. Smith, L. Zhou, W. Kim, G. S. Pulcu *et al.*, Droplet printing reveals the importance of micron-scale structure for bacterial ecology, *Nat. Commun.* **12**, 857 (2021).
- [12] C. M. Hindson, J. R. Chevillet, H. A. Briggs, E. N. Gallichotte, I. K. Ruf, B. J. Hindson, R. L. Vessella, and M. Tewari, Absolute quantification by droplet digital pcr versus analog real-time pcr, *Nat. Methods* **10**, 1003 (2013).
- [13] Y. Zhang, Y. Minagawa, H. Kizoe, K. Miyazaki, R. Iino, H. Ueno, K. V. Tabata, Y. Shimane, and H. Noji, Accurate high-throughput screening based on digital protein synthesis in a massively parallel femtoliter droplet array, *Sci. Adv.* **5**, eaav8185 (2019).
- [14] D. Zaremba, S. Błoński, and P. M. Korczyk, Integration of capillary-hydrodynamic logic circuitries for built-in control over multiple droplets in microfluidic networks, *Lab Chip* **21**, 1771 (2021).
- [15] A. I. Segaliny, G. Li, L. Kong, C. Ren, X. Chen, J. K. Wang, D. Baltimore, G. Wu, and W. Zhao, Functional tcr t cell screening using single-cell droplet microfluidics, *Lab Chip* **18**, 3733 (2018).
- [16] M. Pellegrino, A. Sciambi, S. Treusch, R. Durruthy-Durruthy, K. Gokhale, J. Jacob, T. X. Chen, J. A. Geis, W. Oldham, J. Matthews *et al.*, High-throughput single-cell dna sequencing of acute myeloid leukemia tumors with droplet microfluidics, *Genome Res.* **28**, 1345 (2018).
- [17] M. J. Spindler, A. L. Nelson, E. K. Wagner, N. Oppermans, J. S. Bridgeman, J. M. Heather, A. S. Adler, M. A. Asensio, R. C. Edgar, Y. W. Lim *et al.*, Massively parallel interrogation and mining of natively paired human tcr $\alpha\beta$ repertoires, *Nat. Biotechnol.* **38**, 609 (2020).
- [18] A. Gérard, A. Woolfe, G. Mottet, M. Reichen, C. Castrillon, V. Menrath, S. Ellouze, A. Poitou, R. Doineau, L. Briseno-Roa *et al.*, High-throughput single-cell activity-based screening and sequencing of antibodies using droplet microfluidics, *Nat. Biotechnol.* **38**, 715 (2020).
- [19] T. Thorsen, R. W. Roberts, F. H. Arnold, and S. R. Quake, Dynamic Pattern Formation in a Vesicle-Generating Microfluidic Device, *Phys. Rev. Lett.* **86**, 4163 (2001).
- [20] S. L. Anna, N. Bontoux, and H. A. Stone, Formation of dispersions using flow focusing in microchannels, *Appl. Phys. Lett.* **82**, 364 (2003).
- [21] C. Cramer, P. Fischer, and E. J. Windhab, Drop formation in a co-flowing ambient fluid, *Chem. Eng. Sci.* **59**, 3045 (2004).
- [22] J. H. Xu, S. Li, J. Tan, and G. Luo, Correlations of droplet formation in t-junction microfluidic devices: From squeezing to dripping, *Microfluid. Nanofluid.* **5**, 711 (2008).
- [23] C. N. Baroud, F. Gallaire, and R. Dangla, Dynamics of microfluidic droplets, *Lab Chip* **10**, 2032 (2010).
- [24] P. M. Korczyk, V. Van Steijn, S. Blonski, D. Zaremba, D. A. Beattie, and P. Garstecki, Accounting for corner flow unifies the understanding of droplet formation in microfluidic channels, *Nat. Commun.* **10**, 2528 (2019).

- [25] R. Dangla, E. Fradet, Y. Lopez, and C. N. Baroud, The physical mechanisms of step emulsification, *J. Phys. D* **46**, 114003 (2013).
- [26] M. De menech, P. Garstecki, F. Jousse, and H. A. Stone, Transition from squeezing to dripping in a microfluidic T-shaped junction, *J. Fluid Mech.* **595**, 141 (2008).
- [27] R. Dangla, S. C. Kayi, and C. N. Baroud, Droplet microfluidics driven by gradients of confinement, *Proc. Natl. Acad. Sci. USA* **110**, 853 (2013).
- [28] Z. Li, A. Leshansky, L. Pismen, and P. Tabeling, Step-emulsification in a microfluidic device, *Lab Chip* **15**, 1023 (2015).
- [29] M. L. Eggersdorfer, H. Seybold, A. Ofner, D. A. Weitz, and A. R. Studart, Wetting controls of droplet formation in step emulsification, *Proc. Natl. Acad. Sci. USA* **115**, 9479 (2018).
- [30] X. Niu, F. Gielen, J. B. Edel, and A. J. Demello, A microdroplet dilutor for high-throughput screening, *Nat. Chem.* **3**, 437 (2011).
- [31] F. Lan, J. R. Haliburton, A. Yuan, and A. R. Abate, Droplet barcoding for massively parallel single-molecule deep sequencing, *Nat. Commun.* **7**, 11784 (2016).
- [32] D. R. Link, S. L. Anna, D. A. Weitz, and H. A. Stone, Geometrically Mediated Breakup of Drops in Microfluidic Devices, *Phys. Rev. Lett.* **92**, 054503 (2004).
- [33] M. De Menech, Modeling of droplet breakup in a microfluidic T-shaped junction with a phase-field model, *Phys. Rev. E* **73**, 031505 (2006).
- [34] A. M. Leshansky and L. M. Pismen, Breakup of drops in a microfluidic T junction, *Phys. Fluids* **21**, 023303 (2009).
- [35] S. Afkhami, A. Leshansky, and Y. Renardy, Numerical investigation of elongated drops in a microfluidic t-junction, *Phys. Fluids* **23**, 022002 (2011).
- [36] B. Chen, G. Li, W. Wang, and P. Wang, 3d numerical simulation of droplet passive breakup in a micro-channel t-junction using the volume-of-fluid method, *Appl. Therm. Eng.* **88**, 94 (2015).
- [37] Y. Chen and Z. Deng, Hydrodynamics of a droplet passing through a microfluidic t-junction, *J. Fluid Mech.* **819**, 401 (2017).
- [38] X. Sun, C. Zhu, T. Fu, Y. Ma, and H. Z. Li, Dynamics of droplet breakup and formation of satellite droplets in a microfluidic T-junction, *Chem. Eng. Sci.* **188**, 158 (2018).
- [39] X. Sun, C. Zhu, T. Fu, Y. Ma, and H. Z. Li, Breakup dynamics of elastic droplet and stretching of polymeric filament in a T-junction, *Chem. Eng. Sci.* **206**, 212 (2019).
- [40] M.-C. Jullien, M.-J. Tsang Mui Ching, C. Cohen, L. Menetrier, and P. Tabeling, Droplet breakup in microfluidic t-junctions at small capillary numbers, *Phys. Fluids* **21**, 072001 (2009).
- [41] D. Hoang, L. Portela, C. Kleijn, M. Kreutzer, and V. Van Steijn, Dynamics of droplet breakup in a t-junction, *J. Fluid Mech.* **717**, R4(2013).
- [42] A. M. Leshansky, S. Afkhami, M.-C. Jullien, and P. Tabeling, Obstructed Breakup of Slender Drops in a Microfluidic T Junction, *Phys. Rev. Lett.* **108**, 264502 (2012).
- [43] X. Wang, C. Zhu, Y. Wu, T. Fu, and Y. Ma, Dynamics of bubble breakup with partly obstruction in a microfluidic T-junction, *Chem. Eng. Sci.* **132**, 128 (2015).
- [44] C. Haringa, C. de Jong, D. A. Hoang, L. M. Portela, C. R. Kleijn, M. T. Kreutzer, and V. Van Steijn, Breakup of elongated droplets in microfluidic T-junctions, *Phys. Rev. Fluids* **4**, 024203 (2019).
- [45] J. Chang and J. Cai, Dynamics of obstructed droplet breakup in microfluidic T-junction based on diffuse interface method, *Heat Mass Transf.* **56**, 1601 (2020).
- [46] A. E. M. Mora *et al.*, Numerical study of the dynamics of a droplet in a T-junction microchannel using openfoam, *Chem. Eng. Sci.* **196**, 514 (2019).
- [47] M. Samie, A. Salari, and M. B. Shafii, Breakup of microdroplets in asymmetric T junctions, *Phys. Rev. E* **87**, 053003 (2013).
- [48] A. Bedram, A. Moosavi, and S. K. Hannani, Analytical relations for long-droplet breakup in asymmetric T junctions, *Phys. Rev. E* **91**, 053012 (2015).
- [49] M. Zheng, Y. Ma, T. Jin, and J. Wang, Effects of topological changes in microchannel geometries on the asymmetric breakup of a droplet, *Microfluid. Nanofluid.* **20**, 1 (2016).
- [50] V. van Steijn, P. M. Korczyk, L. Derzsi, A. R. Abate, D. A. Weitz, and P. Garstecki, Block-and-break generation of microdroplets with fixed volume, *Biomicrofluid.* **7**, 024108 (2013).

- [51] H. Wong, S. Morris, and C. Radke, Three-dimensional menisci in polygonal capillaries, *J. Colloid Interface Sci.* **148**, 317 (1992).
- [52] T. C. Ransohoff and C. J. Radke, Laminar flow of a wetting liquid along the corners of a predominantly gas-occupied noncircular pore, *J. Colloid Interface Sci.* **121**, 392 (1988).
- [53] H. A. Stone and L. G. Leal, The effects of surfactants on drop deformation and breakup, *J. Fluid Mech.* **220**, 161 (1990).
- [54] C. D. Eggleton, T.-M. Tsai, and K. J. Stebe, Tip Streaming from a Drop in the Presence of Surfactants, *Phys. Rev. Lett.* **87**, 048302 (2001).
- [55] H. Wong, C. J. Radke, and S. Morris, The motion of long bubbles in polygonal capillaries. Part 1. Thin films, *J. Fluid Mech.* **292**, 71 (1995).
- [56] M. Musterd, V. van Steijn, C. Kleijn, and M. Kreutzer, Calculating the volume of elongated bubbles and droplets in microchannels from a top view image, *RSC Adv.* **5**, 16042 (2015).
- [57] A. de Lózar, A. L. Hazel, and A. Juel, Scaling Properties of Coating Flows in Rectangular Channels, *Phys. Rev. Lett.* **99**, 234501 (2007).
- [58] A. De Lózar, A. Juel, and A. L. Hazel, The steady propagation of an air finger into a rectangular tube, *J. Fluid Mech.* **614**, 173 (2008).
- [59] F. Jousse, G. Lian, R. Janes, and J. Melrose, Compact model for multi-phase liquid-liquid flows in microfluidic devices, *Lab Chip* **5**, 646 (2005).
- [60] D. A. Sessoms, M. Belloul, W. Engl, M. Roche, L. Courbin, and P. Panizza, Droplet motion in microfluidic networks: Hydrodynamic interactions and pressure-drop measurements, *Phys. Rev. E* **80**, 016317 (2009).
- [61] J. Zhou, A. Wei, A. Bertsch, and P. Renaud, High precision, high throughput generation of droplets containing single cells, *Lab Chip* **22**, 4841 (2022).